

Visible-light photocatalytic activity of rare-earth-metal-doped TiO₂: Experimental analysis and machine learning for virtual design

Alicja Mikolajczyk^a, Ewelina Wyrzykowska^a, Paweł Mazierski^{b,c}, Tomasz Grzyb^d, Zhishun Wei^{c,e}, Ewa Kowalska^{c,f}, Pablo Nicolas Caicedo^b, Adriana Zaleska-Medynska^b, Tomasz Puzyn^a, Joanna Nadolna^{b,c,*}

^a Laboratory of Environmental Chemometrics, Faculty of Chemistry, University of Gdańsk, 80–308 Gdańsk, Poland

^b Laboratory of photocatalysis, Department of Environmental Technology, Faculty of Chemistry, University of Gdańsk, 80–308 Gdańsk, Poland

^c Institute for Catalysis, Hokkaido University, Sapporo 001–0021, Japan

^d Department of Rare Earths, Adam Mickiewicz University in Poznań, 61–614 Poznań, Poland

^e Hubei Provincial Key Laboratory of Green Materials for light Industry, Hubei University of Technology, Wuhan 430068, China

^f Faculty of Chemistry, Jagiellonian University, 30–387 Krakow, Poland



ARTICLE INFO

Keywords:

Lanthanide

TiO₂

Photocatalysis

Visible-light photoactivity

Up-conversion

ABSTRACT

Modification with rare-earth (RE) metals has emerged as an important approach for enhancing the properties of titanium dioxide. Herein, the visible-light photocatalytic activity of RE-TiO₂ (RE: Tm, Er, Nd, Dy, Lu, La, Ho, Pr, Tb, Sc, Ce, Yb, Sm, Gd, Y, or Eu) was investigated using a combination of computer simulations and experimental techniques. The RE-TiO₂ photocatalysts were characterised using advanced experimental techniques, including X-ray diffraction, X-ray photoelectron spectroscopy, luminescence, diffuse reflectance spectroscopy, and specific surface area measurements. Furthermore, a quantitative structure–activity relationship analysis was conducted by applying a partial least-squares machine learning algorithm. The Ho-TiO₂ sample exhibited the highest photocatalytic activity under visible-light irradiation. Notably, the observed activity was not due to an up-conversion process, originating instead from slight bandgap narrowing caused by new sub-bandgap states from the RE 4f levels.

1. Introduction

Titanium dioxide (TiO₂) is a versatile material with unique properties such as excellent photocatalytic activity, high chemical stability, and biocompatibility. Consequently, TiO₂ has become a crucial component in various applications, from environmental remediation and energy conversion to cosmetics and biomedical devices. Nevertheless, the efficiency of TiO₂ in certain applications is limited by a relatively wide bandgap and poor visible-light absorption. To address these shortcomings and achieve enhanced performance, research efforts have been focused on modifying TiO₂ with rare-earth (RE) metals [1–5].

RE metals, a group of 17 chemical elements found in the Earth's crust, have intriguing electronic, magnetic, and optical properties. These elements are of significant interest in materials science because of their

ability to influence the electronic structures and optical properties of host materials. The incorporation of RE metals can induce desirable changes in TiO₂, such as narrowing the bandgap, extending the absorption spectrum into the visible region, and enhancing the charge separation and transfer processes [6–13].

Moreover, as dopants, RE metals possess the unique ability to sensitise up-conversion luminescence in host materials. By introducing carefully selected RE ions into TiO₂ matrices, materials that exhibit up-conversion effects can be engineered, facilitating the efficient conversion of near-infrared (NIR) light into visible or ultraviolet (UV) light. This up-conversion process involves a series of sequential photon absorption and emission events, creating the potential for enhanced light harvesting and energy utilisation [14–17].

Although the modification of TiO₂ with RE metals is promising for

Abbreviations: RE, rare-earth; NIR, near-infrared; UV, ultraviolet; XPS, X-ray photoelectron spectroscopy; BET, Brunauer, Emmett, and Teller; XRD, X-ray diffraction; HPLC, high-performance liquid chromatography; QSAR, quantitative structure–activity relationship; PLS, partial least-squares; LV, latent vector; GA, genetic algorithm, DRS, diffuse reflectance spectroscopy; ET, energy transfer; CT, charge transfer; AQE, apparent quantum efficiency.

* Correspondence to: University of Gdańsk, Faculty of Chemistry, Department of Environmental Technology, Jana Bazyskiego 8, 80–309 Gdańsk, Poland.

E-mail address: joanna.nadolna@ug.edu.pl (J. Nadolna).

<https://doi.org/10.1016/j.apcatb.2024.123744>

Received 31 October 2023; Received in revised form 28 December 2023; Accepted 14 January 2024

Available online 18 January 2024

0926-3373/© 2024 Elsevier B.V. All rights reserved.

various applications, the resulting structural and electronic changes are not comprehensively understood. In this study, both computational and experimental techniques were used to elucidate the effects of RE metal doping on TiO_2 , providing insights into the underlying mechanisms and properties of these modified materials. Photocatalysts based on TiO_2 doped with each RE element (Tm, Er, Nd, Dy, Lu, La, Ho, Pr, Tb, Sc, Ce, Yb, Sm, Gd, Y, and Eu), except Pm, were synthesised and characterised for the first time. Pm- TiO_2 was not synthesised owing to the radioactivity of Pm. The results of this interdisciplinary investigation will not only contribute to a deeper understanding of TiO_2 modification with RE metals but also facilitate numerous applications spanning catalysis, energy conversion, and photonics. The synergy between the computational and experimental techniques applied in this study exemplifies the power of multifaceted approaches for advancing materials science and technology.

2. Experimental

2.1. Photocatalyst preparation

The photocatalysts used in this study were synthesised via a hydrothermal method following a previously established procedure [14]. First, solution A was prepared by mixing 16 mL of titanium tetraisopropoxide (97%) and 136 mL of isopropanol in a beaker using a magnetic stirrer for 30 min. Then, solution B was prepared by combining 4.8 mL of water, 4.8 mL of isopropanol, 1.6 mL of HNO_3 (65%), and an appropriate amount of $\text{RE}(\text{NO}_3)_3 \cdot 5\text{H}_2\text{O}$ (0.25 mol%, RE: Tm, Er, Nd, Dy, Lu, La, Ho, Pr, Tb, Sc, Ce, Yb, Sm, Gd, Y, or Eu). After adding solution B to solution A and stirring for 1 h, the mixture was poured into a Teflon-lined autoclave and dried at 120 °C for 4 h. The resulting powder was washed four times with deionised water, recovered by centrifugation (10,000 rpm, 15 min), and dried at 80 °C overnight. The samples were then calcined at 450 °C for 2 h (heating rate: 2 °C/min).

2.2. Characterisation

The properties and chemical compositions of the samples were analysed using various methods. The surface composition was determined by X-ray photoelectron spectroscopy (XPS) using a JEOL JPC-9010MC spectrophotometer with an $\text{MgK}\alpha$ X-ray source (JEOL, Ltd., Tokyo, Japan). Fifty scans were collected for titanium, oxygen, and carbon, whereas 100 scans were required for the precise characterisation of the RE owing to its low content. Luminescence spectra were collected using a Princeton Instruments PIXIS 256E Digital CCD Camera (Trenton, NJ, USA) equipped with an SP-2156 Imaging Spectrograph and Opolette 355LD UVDM tuneable laser as the excitation source. All the spectra were corrected for the instrumental response. The absorption properties were determined using a UV-vis spectrophotometer (UV-2600, Shimadzu, Kyoto, Japan) with barium sulfate as a reference. The specific surface area was determined using the Brunauer, Emmett, and Teller (BET) method based on the nitrogen adsorption-desorption isotherms recorded at –196.15 °C on a Micromeritics Gemini V instrument (Norcross, GA, USA). The crystalline properties were evaluated by powder X-ray diffraction (XRD) using a Rigaku Intelligent XRD SmartLab diffractometer with a Cu target (Rigaku, Ltd., Tokyo, Japan). The 2θ range was 20–80° with a scan speed of 1°/min and step size of 0.01°. The Rigaku PDXL software (v. 2.3) was used to calculate the crystallite sizes using the Scherrer equation, with corrections for the instrument and strain.

2.3. Photocatalytic activity tests

Two irradiation methods were employed for photocatalytic activity testing. First, visible-light activity measurements were performed under polychromatic irradiation using a 1000 W Xe lamp with a water IR filter and Y-420 nm cut-off filter ($\lambda > 400$ nm). Second, for action spectrum

analysis (i.e. under monochromatic irradiation), a diffraction grating-type illuminator (Jasco, RM-FD) fitted with a 300 W Xe lamp (Hamamatsu, C2578-02) was used. These procedures have previously been described in detail [18].

2.3.1. Phenol degradation under polychromatic visible-light irradiation

During photodegradation tests, the reaction system was continuously aerated at 5 dm^3/h and cooled to 10 °C. A mixture of 25 mL of phenol ($C_0 = 0.21$ mM) and 0.125 mg of the photocatalyst was introduced into the photoreactor and subjected to ultrasonic bath treatment for 10 min. Subsequently, the mixture was stirred magnetically for 30 min in the dark to achieve adsorption–desorption equilibrium. Visible irradiation was then initiated, and a 0.5 mL sample was removed from the reactor every 20 min. After filtering (syringe filter, pore size: 0.21 μm), the phenol concentration was determined using high-performance liquid chromatography (HPLC) with a Kinetex C18 column (150 mm × 3 mm; particle size: 2.6 μm ; pore diameter: 100 Å) and an SPD-M20A diode array detector (205, 225, and 254 nm). The mobile phase consisted of acetonitrile and water (7.5/92.5, v/v) at a flow rate of 0.4 mL/min.

2.3.2. Hydroxyl radical ($\bullet\text{OH}$) determination and trapping experiments under polychromatic visible-light irradiation

Hydroxyl radical formation was evaluated using a solution of 5×10^{-4} M of terephthalic acid in 2×10^{-3} M NaOH. This solution produced a highly fluorescent product (2-hydroxyterephthalic acid) upon reaction with hydroxyl radicals. The irradiation procedure was similar to that used for the phenol degradation test, except that the sample volume was 1.7 mL. A luminescence spectrophotometer (PerkinElmer LS 50B, Waltham, MA, USA) was used to measure the fluorescence intensity.

2.3.3. Photocatalytic degradation of phenol in the presence of scavengers under polychromatic visible-light irradiation

Phenol decomposition tests were conducted in the presence of an Er-TiO₂ sample and various scavengers, including benzoquinone, silver nitrate, tert-butanol, and ammonium oxalate. The tests were conducted following the procedure described in Section 2.3.1, with phenol and scavenger concentrations set at $c_0 = 0.21$ M and a 1:1 ratio.

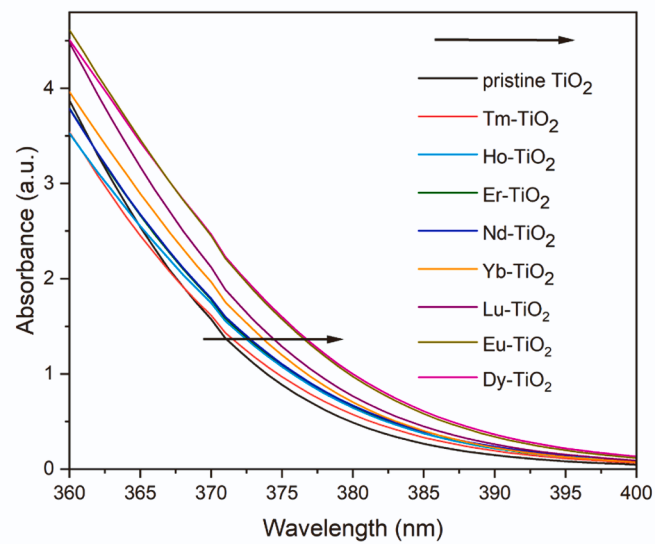
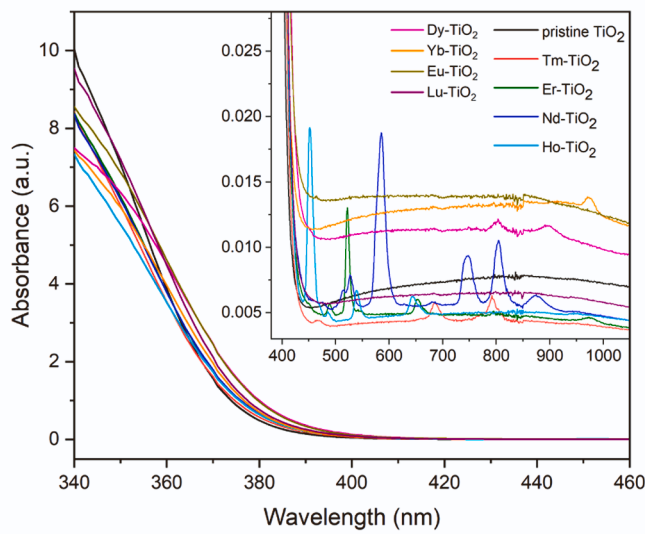
2.3.4. Action spectrum analysis for phenol degradation under monochromatic irradiation

In a quartz cell, 50 mg of the photocatalyst suspended in 5 mL of phenol ($C_0 = 0.21$ M) was subjected to monochromatic irradiation for 90 min while stirring continuously. The irradiation intensity was measured with an optical power metre (HIOKI 3664) and adjusted using a steel mesh to obtain the same value at all tested wavelengths and measured with an optical power metre (HIOKI 3664). During the photocatalytic degradation process, samples were collected every 30 min (1 mL) and filtered. HPLC analysis was conducted using a WAKOSIL-II SC18 AR column (250 mm × 4.6 mm) and the following parameters: flow rate of 1 mL/min; mobile phase of acetonitrile, water, and phosphoric acid (60/39/1, v/v/v); sample injection volume of 5 μL ; and detection at 254 nm. The apparent quantum yield (Φ_{app}) was plotted as a function of the wavelength by calculating the ratio of the electron consumption rate (benzoquinone generation rate) to the incident photon flux, under the assumption that two photons are required based on the reaction stoichiometry.

2.4. Theoretical descriptors of RE-TiO₂

The investigation of photocatalysts was aided by theoretical descriptors derived from the periodic table for RE metals. These descriptors encoded the physicochemical properties and electron structure of RE metals, including molecular weight, molar volume, atomic radius, electronegativity, ionisation potential, HOMO/LUMO energy, electron affinity, and global hardness/softness. These descriptors were collected with the experimental results and used for exploratory analysis and

a)



b)

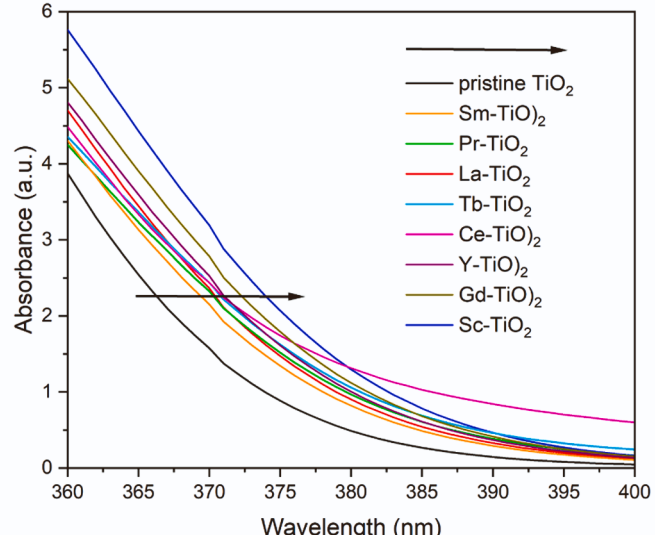
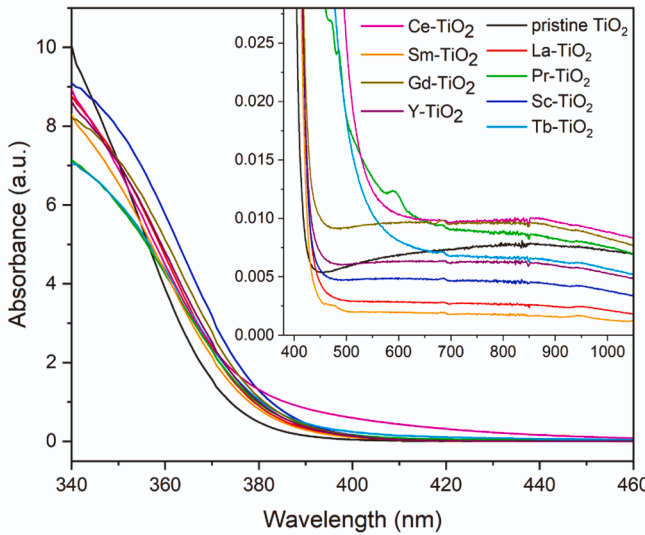


Fig. 1. DRS spectra of RE-TiO₂ and pristine TiO₂ photocatalysts: a) Dy-, Yb-, Eu-, Lu-, Tm-, Er-, Nd-, and Ho-TiO₂; b) Ce-, Sm-, Gd-, Y-, La-, Pr-, Sc-, and Tb-TiO₂.

modelling.

2.5. Computational modelling via partial least-squares analysis supported by a genetic algorithm

The experimental data and theoretical descriptors were explored and the quantitative structure–activity relationship (QSAR) was modelled by applying the partial least-squares (PLS) machine learning algorithm [19]. The PLS method converts the original explanatory variables into new orthogonal variables called latent vectors (LVs), which are constructed to maximise the description of the covariance of the explanatory variables and modelled endpoint. Thus, the first latent vector (LV1) explains the largest amount of covariance, and each subsequent latent vector (LV2, LV3, etc.) explains a smaller portion of the covariance not included in the previous LV. Because each subsequent LV explains a decreased amount of covariance, only the first k LVs contain essential information, and the remaining can be considered noise. The

contribution of the individual original variables to a particular LV is reflected by the loading values, which translate into the values of the coefficients in the mathematical function of the regression model. Thus, the PLS method reduces the multidimensionality of the investigated data while identifying the most relevant original variables based on the loading values. The projection of objects in the analysed feature space adopts the form of a linear map, where the coordinate system consists of the LVs selected for the model. The mechanistic interpretation of the model is based on a comprehensive analysis of the loading values in selected LVs, the regression coefficient value, and the linear map. In this study, the experimental results and theoretical descriptors were transformed into LVs. As the correlation of the LVs with the modelled endpoint did not always align with the increase in covariance, the identification of the most relevant parameters (i.e., experimental and theoretical descriptors) in LVs for the photocatalytic activity of RE-TiO₂ was supported by a genetic algorithm (GA) [20].

The GA belongs to a group of heuristic algorithms, allowing for the

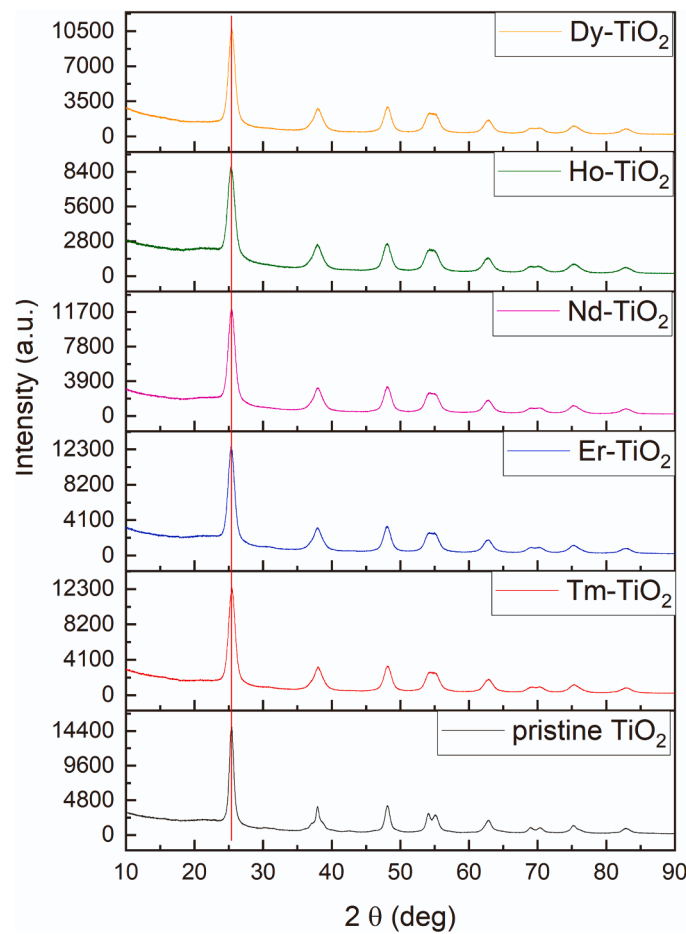


Fig. 2. XRD patterns of selected RE-TiO₂ and pristine TiO₂ photocatalysts.

virtual screening of a wide range of possible solutions for a given issue and identification of the best one. In the GA, the operating principles and terminology are inspired by biological evolution. In other words, the initial population is randomly generated (single-solution proposals of a set of descriptors) from the entire population (all possible solutions). Each solution is evaluated using an objective function that eliminates weaker solutions and selects the best solutions. The objective function is based on the value of Qcv², which is equivalent to R² for the internal validation (cross-validation) system and indicates the robustness of the model. However, during model calibration, statistical parameters reflecting goodness of fit are also calculated, and the solutions (models) with the best configuration of statistics, that is, high and similar values of Qcv² and R², as well as low calibration and cross-validation errors (RMSEc and RMSEcv, respectively), are further processed. These solutions are then subjected to genetic recombination such as crossing and mutations, and a new generation of solutions is created and evaluated. The abovementioned objective function refers to the prediction error for the selected solution, that is, a set of explanatory variables in QSAR modelling, known as descriptors (experimentally or theoretically derived). The GA stops when user-defined conditions are reached; for example, by searching for a certain number of generations of solutions or obtaining a satisfactory value for the objective function (Qcv²).

In this study, the following hyperparameters were used for the GA-PLS combination: number of LVs in the model, 2; number of original variables in the model (descriptors), 7; number of GA iterations, 30; mutation rate, 0.1; initial population size, 200; objective function, R²-Qcv²; and number of folds in cross-validation, 5. Note that before QSAR model development, the experimental data were divided into representative training and validation sets in a 3:1 ratio after sorting by the

phenol degradation percentage. The training set was used to calibrate the model and internal validation system, and the validation set was then used to verify the predictive ability of the developed model. The goodness of fit, robustness, and predictive ability of the model were evaluated according to the generally accepted OECD principles [21].

Because QSAR modelling assumes that the structural similarity between chemicals results in similar activity, the applicability domain of the model was determined using the leverage approach, where the structural similarity of each RE-TiO₂ was coded using a descriptor value [21]. The boundaries of the applicability domain were determined horizontally using the ± 3 standard deviations of the standardised residuals (differences between the experimental and predicted phenol degradation percentage values) and vertically using the critical leverage value calculated based on the number of descriptors in the model and objects in the training set.

3. Results and discussion

3.1. Absorption properties

Diffuse reflectance spectroscopy (DRS) data for the as-prepared RE-TiO₂ samples were collected in range of 340–1050 nm (Fig. 1). Pristine TiO₂ was used as a reference. Each sample exhibits broad and intense absorption below 400 nm, which is assigned to charge transfer (CT) from the O 2p valence band to the Ti 3d conduction band [18]. The absorption edge of each RE-TiO₂ sample is a slightly redshifted compared with that of unmodified TiO₂. This behaviour can be attributed to the CT transition between the RE³⁺ infra-4f electrons and the TiO₂ conduction and valence bands [22]. Absorption bands are observed in the visible–NIR region for the Pr-, Tm-, Er-, Nd-, Ho-, Yb-, and Dy-TiO₂ samples (Fig. 1). The spectra for the Pr-, Tm-, Er-, Nd-, Ho-, and Yb and Dy-TiO₂ samples exhibit additional absorption peaks originating from the f-f electronic transitions of the RE³⁺ ions. The absorption peaks of Pr³⁺ at 470, 486, and 592 nm may be attributable to the transitions from the ³H₄ ground state to the ³P₁, ³P₀, and ¹D₂ excited states, respectively [23]. The absorption peaks of Tm³⁺ at approximately 467, 687, and 795 nm originate from excitation from the ³H₆ ground state to the ¹G₄, ³F_{2/3} and ³H₄ excited states, respectively [24]. The characteristic Er³⁺ absorption peaks at 490, 522, 653, and 973 nm correspond the transitions from the ⁴I_{15/2} ground state to the ⁴F_{7/2}, ²H_{11/2}, ⁴F_{9/2} and ⁴I_{11/2} excited states, respectively [14]. Nd³⁺ exhibits characteristic peaks at 525, 583, 746, 799, and 873 nm, which are correlated to the transitions from the ⁴I_{9/2} ground state to the ²K_{13/2} + ⁴G_{7/2}, ²G_{7/2} + ⁴G_{5/2}, ⁴S_{3/2} + ⁴F_{7/2}, ⁴F_{5/2} + ²H_{9/2}, and ⁴F_{3/2} excited states, respectively [25]. The absorption peaks of Ho³⁺ at approximately 450, 480, 537, and 642 nm originate from the transitions from the ⁵I₈ ground state to the ⁵G₆, ⁵F₃ + ³K₈, ⁵S₂ + ⁵F₄, and ⁵F₅ excited states, respectively [18]. For Yb³⁺, a transition from the ²F_{7/2} ground state to the higher-energy ²F_{5/2} level has been reported at 972 nm [26]. The absorption peaks at 804 and 896 nm are typical of Dy³⁺ and correspond to transitions from the ⁶H_{15/2} ground state to the ⁶F_{9/2} and ⁶F_{7/2} excited states, respectively [20]. These results demonstrate that the selection of an appropriate RE-TiO₂ system results in efficient light harvesting, with photon absorption occurring over a broad range (UV, visible, and NIR).

3.2. Crystalline properties and specific surface area

Fig. 2 shows the XRD patterns of selected RE-TiO₂ and pristine TiO₂ samples. Characteristic diffraction peaks corresponding to the anatase structure appear at 2θ values of 25.4°, 38.0°, 48.2°, 54.2°, and 62.9° (JCPDS NO. 21–1272) [20]. In the XRD patterns of the RE-TiO₂ photocatalysts, the (1 0 1) peak is slightly broader than in that of pristine TiO₂, which may indicate RE³⁺ doping in the TiO₂ crystal lattice [27]. However, the lack of a shift in the XRD peaks (Fig. 2) suggests that only ‘pseudo doping’ (i.e. surface atom replacement) can occur. No secondary phases are observed, suggesting that the concentration of RE-containing

Table 1Physicochemical characterisation of RE-TiO₂ and pristine TiO₂ photocatalysts (standard error: <5%).

Sample label	RE ³⁺ ionic radius (pm)	RE ³⁺ mol. weight (g/mol)	BET surface area (m ² /g)	Phenol degradation (%) under Vis light ($\lambda > 420$ nm) ^a	Reaction rate constant (1/min) under Vis light ($\lambda > 420$ nm) ^a	OH radicals under Vis light ($\lambda > 420$ nm), MAX _{intensity}	Crystallite size (nm)	a=b (Å)	c (Å)	Crystallite volume (Å ³)
Pristine TiO ₂	-	-	106.8	7	0.0009	52	18.8	3.78	9.49	135.75
Tm-TiO ₂	87	168.9	134.4	22	0.0043	41	8.7	3.70	9.51	136.84
Er-TiO ₂	88	167.3	126.6	20	0.0036	38	7.3	3.79	9.51	136.88
Nd-TiO ₂	99	144.2	140.6	23	0.0046	18	8.8	3.78	9.49	136.03
Dy-TiO ₂	91	162.5	131.0	20	0.0036	23	7.1	3.78	9.49	135.84
Lu-TiO ₂	86	175.0	140.7	17	0.0030	28	7.0	3.79	9.50	136.41
La-TiO ₂	106	138.9	135.8	14	0.0027	22	2.9	3.79	9.46	136.00
Ho-TiO ₂	89	164.9	156.6	26	0.0048	23	6.7	3.78	9.49	135.85
Pr-TiO ₂	98	140.9	152.4	8	0.0011	22	6.5	3.79	9.49	135.92
Tb-TiO ₂	92	158.9	148.8	13	0.0023	20	6.7	3.78	9.49	135.83
Sc-TiO ₂	89	44.96	144.0	13	0.0023	29	8.1	3.79	9.51	136.82
Ce-TiO ₂	103	140.1	150.0	13	0.0021	24	8.1	3.79	9.51	136.70
Yb-TiO ₂	86	173.0	141.1	16	0.0030	27	8.3	3.80	9.52	137.20
Sm-TiO ₂	96	150.4	149.7	13	0.0021	22	15.6	3.79	9.49	136.10
Gd-TiO ₂	94	157.3	139.3	15	0.0029	39	8.6	3.80	9.51	137.22
Y-TiO ₂	88	88.91	145.9	14	0.0026	24	5.7	3.78	9.49	135.68
Eu-TiO ₂	95	152.0	151.2	17	0.0030	30	7.7	3.80	9.51	137.24

^a Reference experiments (dark test and phenol photolysis): No phenol degradation during reference experiments.

crystallites is too low for XRD detection. The lattice parameters of the prepared photocatalysts, estimated using the Le Bail method, are summarised in Table 1. The incorporation of RE³⁺ into the TiO₂ matrix is not favourable owing to the large differences between the ionic radii of RE³⁺ ions (0.86–1.06 Å) and Ti⁴⁺ (0.61 Å) [28]. Nevertheless, RE atoms can enter the TiO₂ lattice as interstitial sites, creating Ti–O–RE–O–Ti bonds and expanding the anatase lattice [29]. The Scherrer equation was used to calculate the average crystallite size of the anatase phase. Relative to pristine TiO₂, the RE-TiO₂ samples exhibit an increase in lattice expansion with an increase in crystallite size. Consequently, the RE³⁺ ions are assumed to enter the crystal lattice of TiO₂ or introduce disorder into the lattice.

3.3. Surface composition

The surface compositions of the samples were analysed using XPS (Table 2). The surfaces of all the samples were enriched with carbon (31–64%), which is typical for TiO₂-based materials owing to CO₂ adsorption. For most of the samples, the by O/Ti ratio is similar to the stoichiometric value of 2.0 (TiO₂). A lower value indicates oxygen replacement by RE (doping), whereas a higher value suggests enhanced adsorption of carbon dioxide or water. Indeed, the samples with the largest O/Ti ratios also have the highest carbon contents (e.g. O/Ti ratios of 3.48 and 2.91 for Dy-TiO₂ and Ce-TiO₂ with carbon contents of 64.29% and 49.85%, respectively). In most of the modified samples, the RE content is higher than expected based on the stoichiometric value of 0.25 (RE/Ti), indicating that RE modification mainly occurs on the TiO₂ surface.

To further investigate the surface properties, the three main peaks (Ti 2p_{3/2}, O 1 s, and C 1 s) were deconvoluted. The results are listed in Table S1, and representative spectra are shown in Fig. 3. Titanium is present in two forms, Ti⁴⁺ and Ti³⁺, with four-valent titanium (TiO₂) being predominant, as expected. The oxygen and carbon peaks both have three components. In all the samples, oxygen bound to titanium (TiO₂) is the main form of oxygen. In the case of carbon, C–C bonds are predominant in pristine TiO₂ and four modified samples (Dy-, Ho-, Ce-, and Eu-TiO₂), whereas C–OH is the main carbon species in all the other photocatalysts (Fig. 3). As suggested by the surface composition (Table 2), Dy-TiO₂ has the highest content of adsorbed hydroxyl groups and carbon dioxide (C=O). This sample also has the highest content (5.6%) of reduced titanium (Ti³⁺), indicating that Dy (similar to other RE) disturbs the formation of perfect TiO₂ crystals; thus, doping with Dy

might be expected. However, the lack of shift in the XRD peaks (Fig. 2) suggest that only ‘pseudo doping’ (i.e. surface atom replacement) can occur.

3.4. Photoluminescence

The photoluminescence of the RE-TiO₂ samples under laser excitation at 250 nm was investigated. The photoluminescence spectra varied depending on the RE³⁺ dopant (Fig. S1), confirming the successful doping of TiO₂. The emission of RE³⁺ ions, which originates from 4f–4f electronic transitions, is usually characterised by narrow bands, such as those observed for TiO₂:Sm³⁺ [30,31]. The emission bands are located in the UV–NIR range owing to the energies of the 4f–4f transitions. However, the observation of emission from the RE³⁺ ions requires that transitions can occur within the 4f shell and that the excitation wavelength corresponds to the ion absorption bands or that energy transfer (ET) or CT occurs from the host to the ion [32]. The first condition is not fulfilled by Sc³⁺, Y³⁺, La³⁺, or Lu³⁺, as the first two species do not have 4f electrons, La³⁺ has empty 4f shells, and Lu³⁺ has full 4f shells. Therefore, the spectra of the corresponding RE-TiO₂ samples show only the broad emission of the TiO₂ host. The second condition is met by Nd³⁺, Sm³⁺, Eu³⁺, Tm³⁺, and Yb³⁺, which show emission bands under laser excitation at 250 nm. The remaining RE³⁺ ions are not excited by laser irradiation, and ET from the TiO₂ host is not efficient enough to excite the dopant ions. Therefore, to observe any potential emission from these ions, we used different excitation wavelengths to match the absorption bands of the individual ions (Fig. S2).

The sample doped with Sm³⁺ ions exhibits the highest emission intensity among all samples under 250-nm laser excitation. It is not clear why this particular sample exhibits the best luminescence. Among all lanthanide ions, four ions exhibit the highest Stokes luminescence intensity and quantum yields in the visible range—two to the left of gadolinium in the periodic table, namely Eu³⁺ and Sm³⁺, and two to the right, namely Tb³⁺ and Dy³⁺ [33]. This is due to the electronic structures of these ions [34]. They exhibit significant energy differences between the excited state from which emission occurs and the ground state. Such a large difference also reduces the risk of cross-relaxation between Ln³⁺ ions. Therefore, Sm³⁺ ions must exhibit intense emission. Another factor is the alignment of excitation wavelength with the appropriate absorption band. In this case, laser excitation at a wavelength of 250 nm perfectly aligns with the CT band of O²⁻→Sm³⁺ [35]. Furthermore, the emission peak of the matrix, which is TiO₂ at ~575 nm

Table 2Surface composition of RE-TiO₂ and pristine TiO₂ photocatalysts.

Sample label	RE (at %)	Ti (at %)	O (at %)	C (at %)	O/Ti (at. ratio)	C/Ti (at. ratio)	RE/Ti (at. ratio%)
TiO ₂	-	15.59	34.94	49.47	2.24	3.17	-
Tm-TiO ₂	0.08	20.66	38.13	41.14	1.85	1.99	0.39
Er-TiO ₂	0.07	18.52	36.99	44.42	2.00	2.40	0.38
Nd-TiO ₂	0.07	22.14	39.65	38.14	1.79	1.72	0.32
Dy-TiO ₂	0.03	7.97	27.71	64.29	3.48	8.07	0.38
Lu-TiO ₂	0.04	18.87	36.85	44.24	1.95	2.34	0.21
La-TiO ₂	0.09	21.93	42.14	35.83	1.92	1.63	0.41
Ho-TiO ₂	0.05	12.22	35.52	52.21	2.91	4.27	0.41
Pr-TiO ₂	0.08	23.21	45.91	30.81	1.98	1.33	0.34
Tb-TiO ₂	0.08	17.49	38.06	44.34	2.18	2.54	0.46
Sc-TiO ₂	0.12	17.00	37.27	45.60	2.19	2.68	0.71
Ce-TiO ₂	0.07	14.55	35.53	49.85	2.44	3.43	0.48
Yb-TiO ₂	0.05	17.17	36.96	45.82	2.15	2.67	0.29
Sm-TiO ₂	0.07	13.05	33.43	53.45	2.56	4.10	0.54
Gd-TiO ₂	0.05	20.24	39.78	39.93	1.97	1.97	0.25
Y-TiO ₂	0.08	16.22	34.95	48.74	2.15	3.00	0.49
Eu-TiO ₂	0.05	17.23	35.85	46.87	2.08	2.72	0.29

(~17,300 cm⁻¹; shown in Fig. S1), corresponds to the energy of the ⁴G_{5/2} level of the Sm³⁺ ion (~17,800 cm⁻¹) [34], suggesting efficient ET from TiO₂ to Sm³⁺ for these ions, which are imbedded in the TiO₂ structure. However, the aforementioned properties are not the only causes of intense emission in TiO₂:Sm³⁺ for the discussed materials. High intensity could also be expected in the case of the TiO₂:Eu³⁺ sample (the ⁴D₀ level of the Eu³⁺ ion has an energy of ~17,200 cm⁻¹) [34]. However, the analysis of the composition of the obtained materials presented in Table 2 revealed that the TiO₂:Sm³⁺ sample has one of the highest RE-to-Ti ratios, almost twice as large as that of the TiO₂:Eu³⁺ sample. Therefore, the high content of Sm³⁺ ions also affects the high intensity of emission in this sample.

In addition to the emission of RE³⁺ ions, a broad band appears between 400 and 800 nm, which is typical of TiO₂ host compounds and results from the formation and release of charge carriers and vacancies

[6,24,36]. The shape and number of maxima can vary depending on the synthesis method and the structural or morphological properties of TiO₂ [14,24,36]. The complex structure of the TiO₂ emission band is evident in the pristine sample (Fig. S1). At least three maxima can be distinguished, which vary depending on the RE³⁺ dopant. The intensity of the band at approximately 550 nm, increases with Dy³⁺, Er³⁺, and Lu³⁺ doping. However, this behaviour is somewhat random and likely unrelated to the type of RE³⁺ ion. Because the TiO₂ emission associated with oxygen vacancies with one (F⁻ centres) or two (F⁺ centres) trapped electrons, it is sensitive to the surface chemistry, and the formation of small amounts of RE₂O₃ oxides may affect the observed emission [37]. Additionally, ET from TiO₂ to the RE³⁺ ions can quench the TiO₂ emission or change the emission band characteristics.

Fig. S2 exhibits the emission properties of the RE³⁺ ions doped in the TiO₂ host at the optimal excitation wavelength for each ion. These results demonstrate that ions such as Pr³⁺, Tb³⁺, and Ho³⁺ can be excited, even though no emission is observed upon laser excitation at 250 nm (Fig. S1). Unfortunately, no emission is obtained with Ce³⁺ because this ion has broad f-d-type transitions that occur in the UV range. Furthermore, Gd³⁺ cannot be excited at the selected wavelengths because its emission bands are located at approximately 270 and 310 nm, requiring excitation in the deep-UV range.

The spectra presented in Fig. S2 are typical of the RE³⁺ ions, with most of the transition peaks being located in the visible range. The relatively broad shapes of the observed emission bands may be related to the RE³⁺-containing phase being amorphous or poorly crystallised. Moreover, the multisite distribution of RE³⁺ ions typically broadens the emission bands.

Under laser excitation, no up-conversion luminescence was observed (Nd-TiO₂: 525, 585, 746, 799, and 873 nm; Tm-TiO₂: 467, 687, 795; Er-TiO₂: 490, 522, 653, 973 nm; and Ho-TiO₂: 450, 480, 537, and 642 nm) or was too weak to be measured. This lack of emission may be due to the low efficiency of the ground state absorption and excited state absorption mechanisms that lead to up-conversion luminescence for RE³⁺ ions.

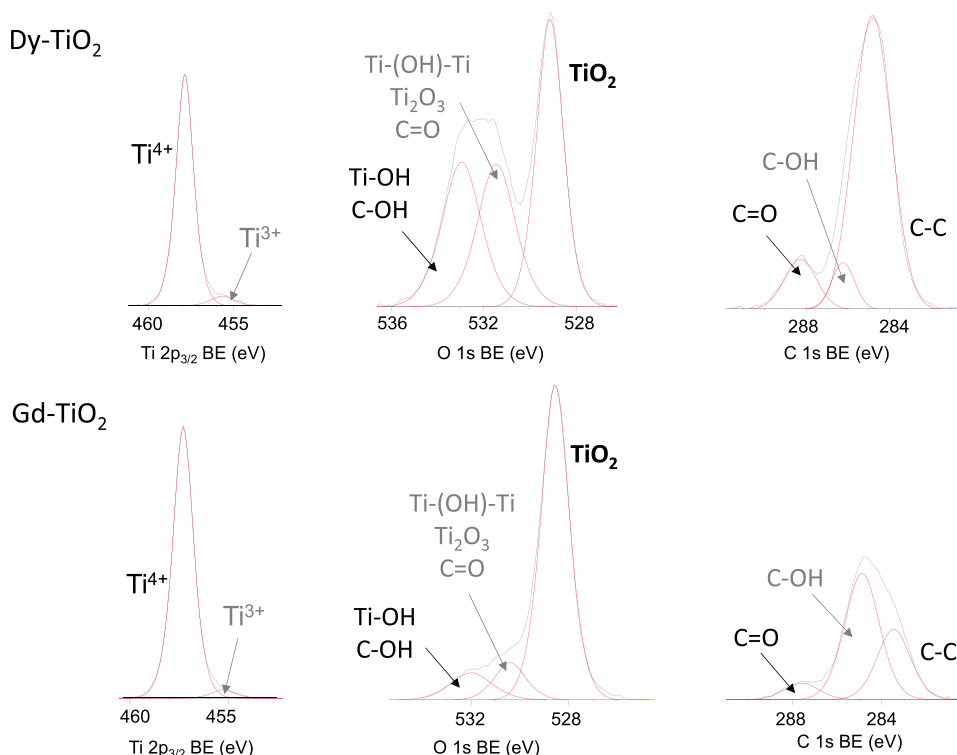


Fig. 3. XPS data for Dy-TiO₂ (top) and Gd-TiO₂ (bottom): deconvoluted Ti 2p_{3/2}, O 1 s, and C 1 s peaks.

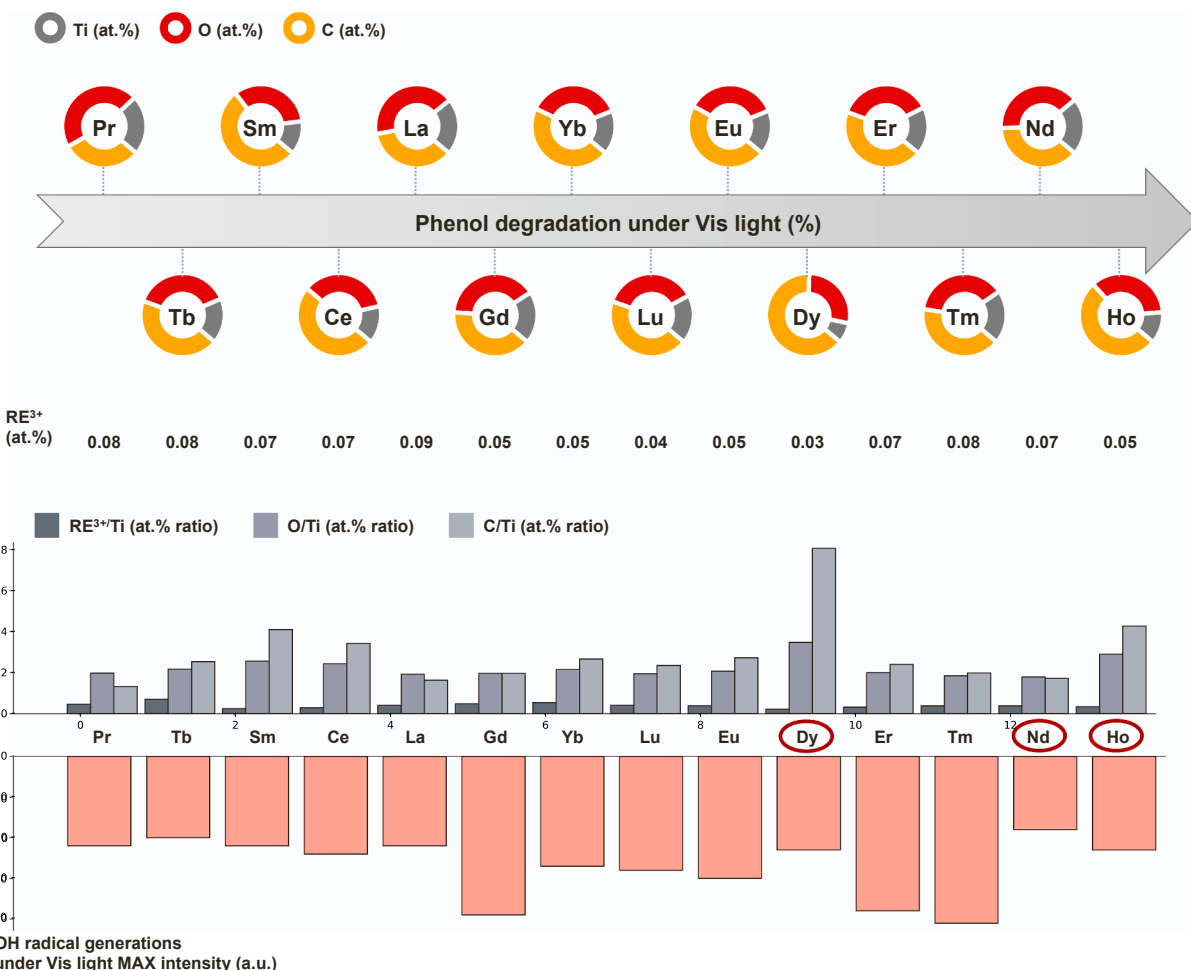


Fig. 4. Visualisation of the phenol degradation properties and OH radical generation ability of the RE-TiO₂ photocatalysts depending on the contents of the individual components (RE³⁺, Ti, O, and C; at%) and their ratios (at% ratio): RE³⁺, Ti, O, C.

3.5. Photocatalytic activity

The ability of the RE-TiO₂ samples to degrade phenol in water under visible-light irradiation ($\lambda > 420$ nm) was examined. The calculated phenol photodegradation efficiencies after irradiation for 60 min and calculated reaction rate constants are presented in Table 1. Reference experiments were performed to assess the effects of the photocatalysts (dark test) and visible-light irradiation (photolysis test) on phenol degradation. The phenol concentration did not decrease during these tests, confirming that the observed activity was due to the photocatalytic pathway. As revealed by the XPS measurements, the pristine TiO₂ sample exhibited carbon enrichment (49 at%) and contained reduced titanium (Ti³⁺). These two parameters may influence the photocatalytic activity of pristine TiO₂ under visible-light irradiation.

All the RE-TiO₂ samples exhibited higher photocatalytic activity than pristine TiO₂. The Pr-TiO₂ sample only exhibited a slight increase in activity (by 1%), likely because only a small amount of Pr was introduced during TiO₂ synthesis. The photocatalytic activity of lanthanide-modified TiO₂ under visible-light irradiation is known to depend on the amount of modifier introduced [23]. The results for the remaining RE-TiO₂ samples can be divided into two groups. The first group is characterised by photoactivities in the range of 10–20% for phenol degradation, and the second group is characterised by photoactivities above 20%. The samples with the best photocatalytic properties are Ho-, Nd-, Tm-, Er-, and Dy-TiO₂, with phenol degradation rates of 26%, 23%, 22%, 20%, and 20%, respectively. In the second group, the photocatalytic activity of the RE-TiO₂ samples decreases in the following

order: Eu = Lu > Yb > Gd > La = Ce = Tb = Sm = Sc. A series of TiO₂ nanotubes modified with Er, Yb, Ho, Tb, Gd, and Pr were synthesised by Mazierski et al. using a two-step electrochemical method [38]. Among the tested samples, TiO₂ nanotubes modified with Ho exhibited the highest activity, achieving a toluene photodegradation rate of 30% after 60 min of visible-light irradiation, similar to our current results.

3.6. Computational modelling

An exploratory experimental data analysis was performed to visualise the photocatalytic activity efficiency (Fig. 4). All the RE-TiO₂ samples were ranked according to the phenol degradation efficiency (grey arrow), and the structural details, including atomic percentages of Ti, O, C, and RE³⁺ as well as their ratios, and the potential for hydroxyl radical (•OH) generation were compared. This analysis confirms the lack of a simple correlation between the quantitative compositions of the RE-TiO₂ samples and the observed phenol degradation behaviour. However, a linear correlation for hydroxyl radical generation is observed for the majority of RE-TiO₂ samples, except Dy-, Nd-, and Ho-TiO₂. As the photocatalytic activity of these samples is assumed to be induced by a mechanism involving a radical species that was not analysed in this study, they were excluded from further QSAR modelling. The remaining RE-TiO₂ samples were divided into training and validation sets according to the 3:1 rule, in which three RE-TiO₂ samples in the training set correspond to one in the validation set. The training set (Pr-TiO₂, Ce-TiO₂, Sc-TiO₂, Tb-TiO₂, La-TiO₂, Y-TiO₂, Yb-TiO₂, Eu-TiO₂, Lu-

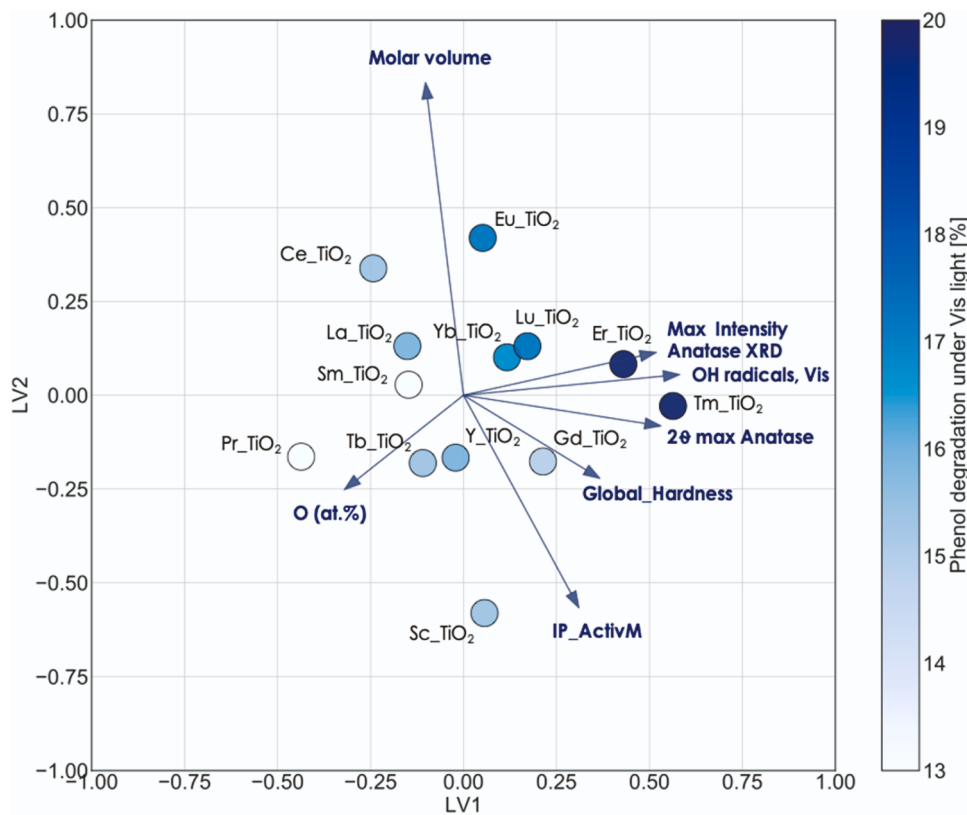


Fig. 5. PLS linear map projected in LV1 and LV2.

TiO₂, and Tm-TiO₂) was used to calibrate the QSAR model, whereas the validation set (Sm-TiO₂, Gd-TiO₂, and Er-TiO₂) allowed verification of its predictive ability.

The applied GA-PLS algorithm indicates the solution with the strongest relationship between a set of original variables and the observed photocatalytic activity based on the selected statistical parameters. The first and second LVs (LV1 and LV2) were relevant and ranked the substantial explanatory variables with coefficients in the regression model (Fig. S3, Eq. 1):

$$\text{Phenol degradation, Vis [\%]} = [14.7] + [1.4]\text{Max. Intensity Anatase XRD} (\text{a.u.}) + [1.3]\text{OH radicals, Vis (a.u.)} + [-1.1]\text{O (at\%)} + [1.0]\text{2θ max Anatase} (\text{o.}) + [1.0]\text{Molar volume [m}^3/\text{mol}] + [0.4]\text{GlobalHardness} + [-0.2]\text{IP_ActivM} \quad (1)$$

Among the most substantial variables, a set of experimentally measured and characterised parameters was identified for the investigated samples (Max. Intensity Anatase XRD, OH radicals, Vis, O content, 2θ max Anatase, and Molar volume). We also identified theoretically calculated descriptors based on periodic properties of the elements that express the potential for interactions, such as the energy of attraction between nucleus and valence electrons in the RE metal atoms (Global Hardness) and ionisation potential (IP_ActivM).

The calculated statistical parameters confirmed the model's goodness of fit (R^2 : 0.987–1, RMSEc: 0.392–0, robustness (Q_{cv}^2): 0.868–1, RMSEcv: 1.26–0), and predictive ability (Q_{ext}^2 : 0.874–1, RMSEext: 1.045–0). The consistency between the experimental and predicted values for phenol degradation by the RE-TiO₂ samples is shown in Fig. S4. Notably, all the RE-TiO₂ samples are inside the applicability domain (Fig. S5). Although the two objects from the validation set are close to or outside the critical leverage value (vertical border), indicating that their structural similarity coded with descriptors differs slightly from that of the samples in the training set, their predictions are still correct (low standardised residuals), and such cases stabilise the

model.

The mechanistic interpretation of the developed QSAR model is based on the overall assessment of the substantial LVs (Fig. S3) and the condensed original variables (Fig. 5). The linear map (Fig. 5) presents the tendency for the RE-TiO₂ photocatalytic activity to increase with LV1, where the highest contributions are provided by hydroxyl radical formation, 2θ max Anatase, and Max. Intensity Anatase XRD. 2θ max Anatase and Max. Intensity Anatase XRD indicate that the most important model factors are correlated with RE doping on the TiO₂ surface, resulting in disorder of the TiO₂ crystal lattice. The linear map does not show clear trends for LV2; thus, the variables included therein (Molar volume and IP_ActivM) have significantly less influence on the photocatalytic activity of the RE-TiO₂ samples. The obtained results are in good agreement with the findings of our previous study, in which we investigated the influence of Er in an Er-TiO₂ system on the electronic properties of the TiO₂(101) structure, and the partial densities of states of Er-TiO₂ and TiO₂ were computed. In this system, Er surface doping of TiO₂ was found to induce the formation of new sub-bandgap states from the Er 4f levels and slight TiO₂ bandgap narrowing [14].

3.7. Photocatalytic mechanism

Selected samples (Tm-, Er-, Ho-, Nd-, Yb-, Eu-, and Dy-TiO₂) were subjected to action spectrum analysis. These samples differ in their photocatalytic activity mechanisms. In the case of Ho-, Er-, Nd-, and Tm-TiO₂, anti-Stokes up-conversion properties could contribute to the photocatalytic activity under visible-light irradiation [6]. The remaining samples (Yb-, Eu-, and Dy-TiO₂) were selected because their photoactivities under visible light are not attributable to the up-conversion phenomenon [40–42]. Fig. 6 shows the apparent quantum efficiency (AQE) as a function of irradiation wavelength. All the investigated RE-TiO₂ samples exhibit a significantly higher AQE than pristine TiO₂. Furthermore, all the tested samples share a similar irradiation range in which they are photoactive. The AQE at an excitation wavelength of

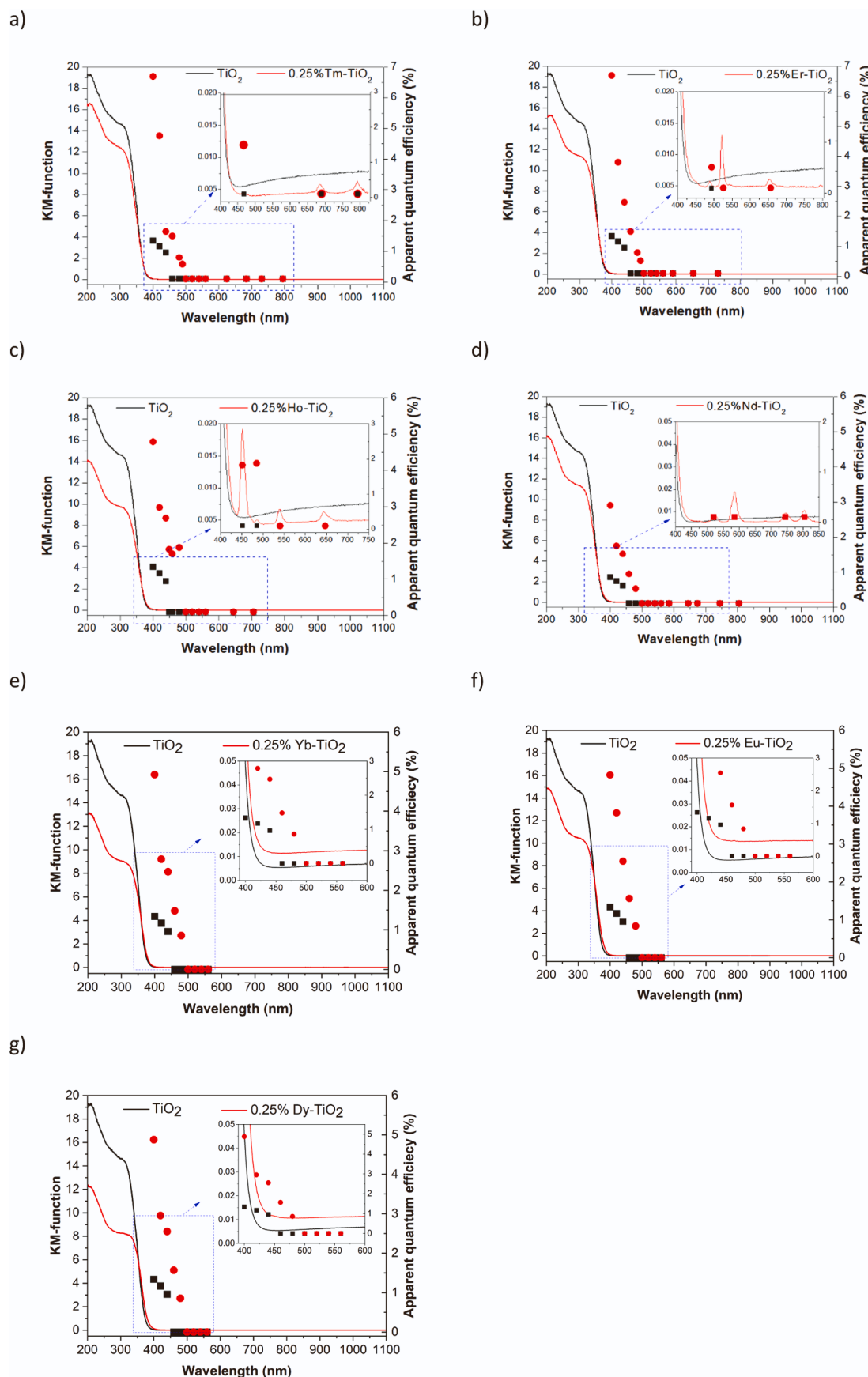


Fig. 6. AQE as a function of irradiation wavelength for: a) Tm-, b) Er-, c) Ho-, d) Nd-, e) Yb-, f) Eu-, and g) Dy-TiO₂ photocatalysts.

500 nm reaches 0%, regardless of the type of RE³⁺ ion. However, the AQE values of the samples differ, decreasing in the following order at an excitation wavelength of 420 nm: Tm, Er, Eu, Ho, Yb, Dy, and Nd.

The photocatalytic activity was also examined for the hydroxyl radical generation reaction, as determined by the maximum intensity of the recorded peak (Table 1). No correlation was observed between the efficiency of phenol degradation and the number of hydroxyl radicals generated on the surface of irradiated TiO₂ (Table 1). The highest intensity was recorded for pristine TiO₂, which exhibited the lowest photocatalytic activity for phenol degradation. These results suggest that the degradation of phenol via hydroxyl radicals is not the predominant pathway for all the RE-TiO₂ samples, and other reactive oxygen species, such as O₂^{•-} may play a crucial role.

Tests on the phenol degradation process in the presence of scavengers were conducted (Fig. S6) to determine the active species responsible for the photocatalytic activity of the Er-TiO₂ photocatalyst. In this study, benzoquinone (O₂^{•-} scavenger), silver nitrate (e⁻ scavenger), tert-butanol (•OH scavenger), and ammonium oxalate (h⁺ scavenger) were introduced into the phenol solution. The results indicated that O₂^{•-} radicals primarily contribute to the phenol degradation process. The phenol degradation process in the presence of •OH and h⁺ scavengers remained consistent in the process without scavengers. A similar correlation for Er- or Ho-modified TiO₂ was confirmed in previous experiments [18,39].

Based on the above experimental and theoretical results, the improved photocatalytic performance of all the RE-TiO₂ samples can predominantly be attributed to the formation of novel sub-bandgap states from the RE 4f levels, resulting from the incorporation of RE dopants on the TiO₂ surface, as confirmed by XRD, XPS and luminescence analyses. Importantly, the up-conversion process did not affect the photocatalytic activity under visible-light irradiation and the oxidation of organic pollutants mostly involved O₂[•] active species.

4. Conclusions

In summary, efficient RE-TiO₂ photocatalysts (RE: Tm, Er, Nd, Dy, Lu, La, Ho, Pr, Tb, Sc, Ce, Yb, Sm, Gd, Y, and Eu) were successfully prepared using a simple hydrothermal method. A combination of computer simulations and experimental studies clarified the effects of RE metal ions on the photocatalytic activity of TiO₂ under visible-light irradiation. The computational study, which employed QSAR analysis conducted by applying the PLS machine learning algorithm, indicated that RE doping on the TiO₂ surface and the resulting disorder in the TiO₂ lattice crystal were responsible for the photocatalytic activity of RE-TiO₂ under visible-light irradiation. Moreover, RE doping on the TiO₂ surface caused the formation of new sub-bandgap states from the RE 4f levels within the bandgap of the TiO₂ system, which may be crucial for photocatalytic activity.

CRediT authorship contribution statement

Wyrzykowska Ewelina: Investigation, Methodology, Software, Visualization, Writing – original draft, Writing – review & editing. **Mikolajczyk Alicja:** Investigation, Methodology, Software, Visualization, Writing – original draft. **Grzyb Tomasz:** Investigation, Methodology, Visualization, Writing – original draft, Writing – review & editing. **Mazierski Paweł:** Investigation, Methodology, Visualization, Writing – original draft. **Puzyn Tomasz:** Resources, Writing – review & editing. **Zaleska-Medynska Adriana:** Resources, Writing – review & editing. **Nadolna Joanna:** Conceptualization, Data curation, Funding acquisition, Investigation, Project administration, Resources, Software, Supervision, Visualization, Writing – original draft, Writing – review & editing. **Wei Zhishun:** Investigation, Visualization, Writing – original draft. **Caicedo Pablo Nicolas Arellano:** Investigation. **Kowalska Ewa:** Resources, Writing – original draft.

Declaration of Competing Interest

The authors declare the following financial interests/personal relationships which may be considered as potential competing interests: Joanna Nadolna reports financial support was provided by National Science Centre Poland.

Data availability

Data will be made available on request.

Acknowledgements

This research was financially supported by Polish National Science Centre (grant No. NCN 2015/17/D/ST5/01331) and by University of Gdańsk (UGrants Project No. 1220/13/2023). Authors would like to highly acknowledge Professor Bunsho Ohtani from ICAT, Japan, for the possibility of conducting research and fruitful discussion.

Appendix A. Supporting information

Supplementary data associated with this article can be found in the online version at doi:10.1016/j.apcatb.2024.123744.

References

- [1] S. Bingham, W.A. Daoud, Recent advances in making nano-sized TiO₂ visible-light active through rare-earth metal doping, *J. Mater. Chem.* 21 (2011) 2041–2050, <https://doi.org/10.1039/C0JM02271C>.
- [2] M. Alhaddad, A.A. Ismail, Y.G. Alghamdi, N.D. Al-Khathami, R.M. Mohamed, Fabrication of novel neodymium oxide coupled mesoporous titania for effective visible light-induced photocatalyst for decomposition of Ciprofloxacin, *Opt. Mater. (Amst.)* 131 (2022) 112579, <https://doi.org/10.1016/j.optmat.2022.112579>.
- [3] E. Cerrato, E. Gaggero, P. Calza, M.C. Paganini, The role of Cerium, Europium and Erbium doped TiO₂ photocatalysts in water treatment: a mini-review, *Chem. Eng. J. Adv.* 10 (2022) 100268, <https://doi.org/10.1016/j.cej.a.2022.100268>.
- [4] Y. Kumari, L.K. Jangir, A. Kumar, M. Kumar, K. Awasthi, Luminescent and structural behaviour of Tb³⁺ ions doped TiO₂ nanoparticles synthesized by facile sol-gel method, *Phys. B Condens Matter* 602 (2021) 412465, <https://doi.org/10.1016/j.physb.2020.412465>.
- [5] Z.N. Kayani, S. Rahim, R. Sagheer, S. Riaz, S. Naseem, Assessment of antibacterial and optical features of sol-gel dip coated La doped TiO₂ thin films, *Mater. Chem. Phys.* 250 (2020) 123217, <https://doi.org/10.1016/j.matchemphys.2020.123217>.
- [6] P. Mazierski, A. Mikolajczyk, B. Bajorowicz, A. Malankowska, A. Zaleska-Medynska, J. Nadolna, The role of lanthanides in TiO₂-based photocatalysis: a review, *Appl. Catal. B* 233 (2018), <https://doi.org/10.1016/j.apcatb.2018.04.019>.
- [7] A. Ahmed, A. Singh, A. Sharma, Prerna, S. Verma, S. Mahajan, S. Arya, Investigating the thermographical effect on optical properties of Eu doped Y2O₃: TiO₂ nanocomposite synthesized via sol-gel method, *Solid State Sci.* 116 (2021) 106617, <https://doi.org/10.1016/j.solidstatosciences.2021.106617>.
- [8] C. Alberoni, I. Barroso-Martín, A. Infantes-Molina, E. Rodríguez-Castellón, A. Talon, H. Zhao, S. You, A. Vomiero, E. Moretti, Ceria doping boosts methylene blue photodegradation in titania nanostructures, *Mater. Chem. Front* 5 (2021) 4138–4152, <https://doi.org/10.1039/D1QM00068C>.
- [9] F.H. Alkallas, T.A. AL-Rebdi, Sh.A. Mansour, Structural and diffuse reflectance investigation of dysprosium-doped TiO₂ nanopowder synthesized by sonochemical hydrolysis technique, *Phys. B Condens Matter* 603 (2021) 412664, <https://doi.org/10.1016/j.physb.2020.412664>.
- [10] J.A. Borrego-Pérez, F. González, C.A. Meza-Avendaño, I.M. De Los Santos, R. López-Juárez, I. Hernández, E.M. Alonso-Guzmán, W. Martínez-Molina, H. L. Chavez-García, Structural, optical and photoluminescence properties of TiO₂ and TiO₂: Tm³⁺ nanopowders, *Opt. (Stuttg.)* 227 (2021) 166083, <https://doi.org/10.1016/j.jleo.2020.166083>.
- [11] M.T. Colomer, K.J. Duarte, A.L. Ortiz, D.F. Mercado, L.M. Ballesteros-Rueda, Influence of Pr³⁺ doping on the synthesis of colloidal sols and nanoparticulate TiO₂ xerogels and their photocatalytic activity, *Mater. Charact.* 182 (2021) 111536, <https://doi.org/10.1016/j.matchar.2021.111536>.
- [12] P. Pascariu, C. Cojocaru, M. Homocianu, P. Samoilă, Tuning of Sm³⁺ and Er³⁺-doped TiO₂ nanofibers for enhancement of the photocatalytic performance: optimization of the photodegradation conditions, *J. Environ. Manag.* 316 (2022) 115317, <https://doi.org/10.1016/j.jenvman.2022.115317>.
- [13] J. Prakash, Samriti, A. Kumar, H. Dai, B.C. Janegitz, V. Krishnan, H.C. Swart, S. Sun, Novel rare earth metal-doped one-dimensional TiO₂ nanostructures: fundamentals and multifunctional applications, *Mater. Today Sustain.* 13 (2021) 10066, <https://doi.org/10.1016/j.mtsust.2021.10066>.
- [14] P. Mazierski, A. Mikolajczyk, T. Grzyb, P.N.A. Caicedo, Z. Wei, E. Kowalska, H. Pinto, A. Zaleska-Medynska, J. Nadolna, On the excitation mechanism of visible

- responsible Er-TiO₂ system proved by experimental and theoretical investigations for boosting photocatalytic activity, *Appl. Surf. Sci.* 527 (2020) 146815, <https://doi.org/10.1016/j.apsusc.2020.146815>.
- [15] E. Akman, S. Akin, T. Ozturk, B. Gulveren, S. Sonmezoglu, Europium and terbium lanthanide ions co-doping in TiO₂ photoanode to synchronously improve light-harvesting and open-circuit voltage for high-efficiency dye-sensitized solar cells, *Sol. Energy* 202 (2020) 227–237, <https://doi.org/10.1016/j.solener.2020.03.108>.
- [16] D. Avram, A.A. Patrascu, M.C. Istrate, B. Cojocaru, C. Tiseanu, Lanthanide doped TiO₂: coexistence of discrete and continuous dopant distribution in anatase phase, *J. Alloy. Compd.* 851 (2021) 156849, <https://doi.org/10.1016/j.jallcom.2020.156849>.
- [17] P. Parnicka, W. Lisowski, T. Klimczuk, J. Łuczak, A. Źak, A. Zaleska-Medynska, Visible-light-driven lanthanide-organic-frameworks modified TiO₂ photocatalysts utilizing up-conversion effect, *Appl. Catal. B* 291 (2021) 120056, <https://doi.org/10.1016/j.apcatb.2021.120056>.
- [18] P. Parnicka, P. Mazierski, T. Grzyb, Z. Wei, E. Kowalska, B. Ohtani, W. Lisowski, T. Klimczuk, J. Nadolna, Preparation and photocatalytic activity of Nd-modified TiO₂ photocatalysts: insight into the excitation mechanism under visible light, *J. Catal.* 353 (2017), <https://doi.org/10.1016/j.jcat.2017.07.017>.
- [19] S. Sengottiyam, A. Mikolajczyk, K. Jagiełło, M. Swirot, T. Pubyn, Core, coating, or corona? The importance of considering protein coronas in nano-QSPR modeling of zeta potential, *ACS Nano* 17 (2023) 1989–1997, <https://doi.org/10.1021/acsnano.2c06977>.
- [20] P. Mazierski, J.K. Roy, A. Mikolajczyk, E. Wyrzykowska, T. Grzyb, P.N.A. Caicedo, Z. Wei, E. Kowalska, A. Zaleska-Medynska, J. Nadolna, Systematic and detailed examination of NaYF₄-Er-Yb-TiO₂ photocatalytic activity under Vis-NIR irradiation: experimental and theoretical analyses, *Appl. Surf. Sci.* 536 (2021) 147805, <https://doi.org/10.1016/j.apsusc.2020.147805>.
- [21] A. Mikolajczyk, A. Gajewicz, B. Rasulev, N. Schaeublin, E. Maurer-Gardner, S. Hussain, J. Leszczynski, T. Pubyn, Zeta potential for metal oxide nanoparticles: a predictive model developed by a nano-quantitative structure–property relationship approach, *Chem. Mater.* 27 (2015) 2400–2407, <https://doi.org/10.1021/cm504406a>.
- [22] P. Parnicka, W. Lisowski, T. Klimczuk, J. Łuczak, A. Źak, A. Zaleska-Medynska, Visible-light-driven lanthanide-organic-frameworks modified TiO₂ photocatalysts utilizing up-conversion effect, *Appl. Catal. B* 291 (2021) 120056, <https://doi.org/10.1016/j.apcatb.2021.120056>.
- [23] J. Reszczynska, T. Grzyb, Z. Wei, M. Klein, E. Kowalska, B. Ohtani, A. Zaleska-Medynska, Photocatalytic activity and luminescence properties of RE³⁺-TiO₂<2</inf> nanocrystals prepared by sol-gel and hydrothermal methods, *Appl. Catal. B*, 181 (2016), <https://doi.org/10.1016/j.apcatb.2015.09.001>.
- [24] P. Mazierski, P.N. Arellano Caicedo, T. Grzyb, A. Mikolajczyk, J.K. Roy, E. Wyrzykowska, Z. Wei, E. Kowalska, T. Pubyn, A. Zaleska-Medynska, J. Nadolna, Experimental and computational study of Tm-doped TiO₂<2</inf>: the effect of Li⁺ on Vis-response photocatalysis and luminescence, *Appl. Catal. B* 252 (2019), <https://doi.org/10.1016/j.apcatb.2019.03.051>.
- [25] P. Parnicka, P. Mazierski, T. Grzyb, W. Lisowski, E. Kowalska, B. Ohtani, A. Zaleska-Medynska, J. Nadolna, Influence of the preparation method on the photocatalytic activity of Nd-modified TiO₂, *Beilstein J. Nanotechnol.* 9 (2018), <https://doi.org/10.3762/bjnano.9.43>.
- [26] V. Singh, K.V. Dabre, S.J. Dhoble, G. Lakshminarayana, Green emitting holmium (Ho) doped yttrium oxide (Y₂O₃) phosphor for solid state lighting, *Opt. (Stuttg.)* 206 (2020) 164339, <https://doi.org/10.1016/j.ijleo.2020.164339>.
- [27] J.S. Revathy, N.S.C. Priya, K. Sandhya, D.N. Rajendran, Structural and optical studies of cerium doped gadolinium oxide phosphor, *Bull. Mater. Sci.* 44 (2021) 13, <https://doi.org/10.1007/s12034-020-02299-w>.
- [28] P. Parnicka, T. Grzyb, A. Mikolajczyk, K. Wang, E. Kowalska, N. Steinfeldt, M. Klein, P. Mazierski, A. Zaleska-Medynska, J. Nadolna, Experimental and theoretical investigations of the influence of carbon on a Ho³⁺-TiO₂ photocatalyst with Vis response, *J. Colloid Interface Sci.* 549 (2019) 212–224, <https://doi.org/10.1016/j.jcis.2019.04.074>.
- [29] K.A. Ali, A.Z. Abdullah, A.R. Mohamed, Visible light responsive TiO₂ nanoparticles modified using Ce and La for photocatalytic reduction of CO₂: Effect of Ce dopant content, *Appl. Catal. A Gen.* 537 (2017) 111–120, <https://doi.org/10.1016/j.apcata.2017.03.022>.
- [30] T. Grzyb, A. Tymiński, Up-conversion luminescence of GdOF:Yb³⁺,Ln³⁺ (Ln = Ho, Tm, Er) nanocrystals, *J. Alloy. Compd.* 660 (2016) 235–243, <https://doi.org/10.1016/j.jallcom.2015.11.122>.
- [31] P.G. Chavan, S.V. Shende, D.S. Joag, M.A. More, Photo-enhanced field emission study of TiO₂ nanotubes array, *Ultramicroscopy* 111 (2011) 415–420, <https://doi.org/10.1016/j.ultramic.2010.11.001>.
- [32] F.Z. Haque, R. Nandanwar, P. Singh, Evaluating photodegradation properties of anatase and rutile TiO₂ nanoparticles for organic compounds, *Opt. (Stuttg.)* 128 (2017) 191–200, <https://doi.org/10.1016/j.ijleo.2016.10.025>.
- [33] J.-C.G. Bünzli, S.V. Eliseeva, Basics of Lanthanide Photophysics, in: P. Hänninen, H. Härmä (Eds.), *Lanthanide Luminescence: Photophysical, Analytical and Biological Aspects*, Springer, Berlin Heidelberg, Berlin, Heidelberg, 2011, pp. 1–45, https://doi.org/10.1007/4243_2010_3.
- [34] W.T. Carnall, H. Crosswhite, H.M. Crosswhite, Energy level structure and transition probabilities in the spectra of the trivalent lanthanides in LaF₃, United States, 1978, <https://doi.org/10.2172/6417825>.
- [35] Y. Hua, J.-U. Kim, J.S. Yu, Charge transfer band excitation of La₃NbO₇:Sm³⁺ phosphors induced abnormal thermal quenching toward high-sensitivity thermometers, *J. Am. Ceram. Soc.* 104 (2021) 4065–4074, <https://doi.org/10.1111/jace.17805>.
- [36] D. Li, H. Haneda, S. Hishita, N. Ohashi, Visible-light-driven N–F–codoped TiO₂ photocatalysts. 2. Optical characterization, photocatalysis, and potential application to air purification, *Chem. Mater.* 17 (2005) 2596–2602, <https://doi.org/10.1021/cm049099p>.
- [37] S. Obregon, A. Kubacka, M. Fernández-García, G. Colón, High-performance Er³⁺-TiO₂ system: dual up-conversion and electronic role of the lanthanide, *J. Catal.* 299 (2013) 298–306, <https://doi.org/10.1016/j.jcat.2012.12.021>.
- [38] P. Mazierski, W. Lisowski, T. Grzyb, M.J. Winiarski, T. Klimczuk, A. Mikolajczyk, J. Flisikowski, A. Hirsch, A. Kołakowska, T. Pubyn, A. Zaleska-Medynska, J. Nadolna, Enhanced photocatalytic properties of lanthanide-TiO₂<2</inf>-nanotubes: an experimental and theoretical study, *Appl. Catal. B* 205 (2017), <https://doi.org/10.1016/j.apcatb.2016.12.044>.
- [39] X. Ren, H. Yao, R. Tang, R. A. S. Yuan, W. Wang, I.M. Ali, Z.-H. Hu, Modification of TiO₂ by Er³⁺ and rGO enhancing visible photocatalytic degradation of arsanilic acid, *Environ. Sci. Pollut. Res.* 30 (2023) 35023–35033, <https://doi.org/10.1007/s11356-022-24627-9>.
- [40] C. Amor, K. Elghniji, E. Elaloui, Improving charge separation, photocurrent and photocatalytic activities of Dy-doped TiO₂ by surface modification with salicylic acid, *J. Mater. Sci. Mater. Electron.* 31 (2020) 1–13, <https://doi.org/10.1007/s10854-020-04606-x>.
- [41] V. Serga, R. Burve, A. Krumina, V. Pankratova, A.I. Popov, V. Pankratov, Study of phase composition, photocatalytic activity, and photoluminescence of TiO₂ with Eu additive produced by the extraction-pyrolytic method, *J. Mater. Res. Technol.* 13 (2021) 2350–2360, <https://doi.org/10.1016/j.jmrt.2021.06.029>.
- [42] M. Pal, U. Pal, R. Silva Gonzalez, E. Sanchez Mora, P. Santiago, Synthesis and photocatalytic activity of Yb doped TiO₂ nanoparticles under visible light, *J. Nano Res.* 5 (2009) 193–200, <https://doi.org/10.4028/www.scientific.net/JNanoR.5.193>.